NUCL SCI TECH (2022) 33:136
https://doi.org/10.1007/s41365-022-01128-5

Prototype of single-event effect localization system with CMOS pixel sensor

Jun Liu[1] · Zhuo Zhou[1] · Dong Wang[1] · Shi-Qiang Zhou[1] · Xiang-Ming Sun[1] · Wei-Ping Ren[1] · Bi-Hui You[1] · Chao-Song Gao[1] · Le Xiao[1] · Ping Yang[1] · Di Guo[1] · Guang-Ming Huang[1] · Wei Zhou[2] · Cheng-Xin Zhao[2,3] · Min Wang[1]

Received: 7 June 2022 / Revised: 20 August 2022 / Accepted: 21 September 2022 / Published online: 8 November 2022

Abstract The single-event effect (SEE) is a serious threat to electronics in radiation environments. The most important issue in radiation-hardening studies is the localization of the sensitive region in electronics to the SEE. To solve this problem, a prototype based on a complementary metal oxide semiconductor (CMOS) pixel sensor, i.e., Topmetal-M, was designed for SEE localization. A beam test was performed on the prototype at the radiation terminal of the Heavy Ion Research Facility in Lanzhou (HIRFL). The results indicated that the inherent deflection angle of the prototype to the beam was 1.7°, and the angular resolution was 0.6°. The prototype localized heavy ions with a position resolution of 3.4 μm.

Keywords Single-event effect · Radiation resistant · Topmetal-M

This work was supported by the National Natural Science Foundation of China (No.U1932143), the National Key Research and Development Program of China (No. 2020YFE0202002), the National Natural Science Foundation of China (Nos. 11875146, 11927901, 12075099, 12075100, 11875145, U2032209), and the Strategic Priority Research Program of Chinese Academy of Sciences (No. XDB34000000).

✉ Dong Wang
dongwang@mail.ccnu.edu.cn

✉ Shi-Qiang Zhou
zsyfsj@mails.ccnu.edu.cn

1 PLAC, Key Laboratory of Quark & Lepton Physics (MOE), Central China Normal University, Wuhan 430079, China

2 Institute of Modern Physics, Chinese Academy of Sciences, Lanzhou 730000, China

3 School of Nuclear Science and Technology, University of Chinese Academy of Sciences, Beijing 100049, China

1 Introduction

Electronics used in aerospace, nuclear reactors, weapons communities, and particle accelerators must be exposed to radiation. This leads to radiation effects, including the single-event effect (SEE) and total ionizing dose [1–4]. These effects can result in incorrect operation and, more seriously, damage the electronics. Thus, radiation-hardening electronics are integral in these fields.

For improving the radiation-hardening ability of electronics, one of the significant steps are to accurately localize the sensitive region on the electronics. Considerable research has been performed in this area. There are three common methods for SEE localization: pulsed laser technology, heavy-ion microbeam technology, and beam penetration technology [5]. In pulsed laser technology, the setup consists of the following major parts: a laser source, a variable attenuator, a focusing unit with an illuminator, a charge-coupled device camera, a positioning system (XYZ stage), and control equipment [6]. The laser emitted from the laser source is focused onto a spot with a diameter of approximately 1 μm to irradiate the device under test (DUT). The DUT is mounted on a three-dimensional positioning system, allowing a submicron displacement resolution. By moving the positioning system, the entire DUT can be irradiated. Studies have indicated that the spatial resolution of pulsed laser technology is approximately 0.5 μm [7, 8]. Pulsed laser technology has the advantages of a low cost, a high temporal resolution, a high spatial resolution, and high-density charge injection. However, the significantly different interactions between photons (absorption) and ionizing particles (Coulomb interactions) make global correlations between laser and heavy-ion tests difficult [9, 10]. Heavy-ion microbeams have been useful for studying the microscopic sensitive areas of electronics to SEEs. They allow precisely defined quantities of ions to be introduced at a precisely defined location. Heavy-ion microbeam technology mainly focuses on ion beams with a spot size of several microns or even smaller and has a spatial resolution of approximately 1 µm [11–14]. The beam is magnetically scanned, and the DUT is irradiated by beam scanning. This technology requires precise control of the movement of the beam spot through the magnet. It has the disadvantages of a complex system, high cost, long scanning time, and low efficiency. In beam penetration technology, the beam positioning chip is typically placed in front of the DUT, and the two chips are placed in parallel. The relative position information between the positioning chip and DUT should be obtained before the test. The beam passes through the positioning chip and hits the DUT. The sensitive region of the DUT is determined through the high-resolution ability of the beam positioning chip [5]. The locating system is simple, and the location accuracy and efficiency of this technology are high.

Monolithic active pixel sensors (MAPS) integrate sensors and readout circuits on a single chip [15]. They have the advantages of a high spatial resolution, high time resolution, high radiation tolerance, and low material budget and are often used for tracking in high-energy physics experiments. Two well-known MAPS chips are Mimosa [16, 17], which was developed for the upgrade of the vertex detector of the STAR experiment, and ALPIDE [18, 19], which was developed for the inner tracking system of the ALICE experiment. Compared with these two chips, Topmetal-M [20, 21]-a MAPS designed by our team for high-energy experiments-has not only spatial resolution but also energy resolution. Thus, it provides more information about the ions. In this study, a prototype based on Topmetal-M for SEE localization was designed, and preliminary tests were conducted at HIRFL. The results indicated that the inherent deflection angle of the prototype to the beam was 1.7°, and the angular resolution was 0.6°. The prototype can also localize heavy ions with a position resolution of 3.4 μm.

2 Working principle of prototype

The principle of the SEE-locating prototype is shown in Fig. 1. It consists of three main parts: the positioning chip Topmetal-M, DUT, and data acquisition system (DAQ). Topmetal-M and the DUT were mounted on two different printed circuit boards. Mechanical tooling was used to install the two boards. This ensured that the two boards were parallel. Thus, Topmetal-M and the DUT were parallel. There were reference points for the mechanical tooling of the two boards. The coordinates of the reference points were fixed. A three-coordinate measuring machine was used to measure the coordinates of the DUT and positioning chip to their corresponding reference points. Using this method, the relative position between Topmetal-M and the DUT was determined before the beam test. Heavy ions were emitted from the terminal, passed through the air, and first hit Topmetal-M. The ions lost part of their energy and generated electron-hole pairs when interacting with Topmetal-M. The electrons were collected and read out by the pixels around the hit point. Subsequently, a cluster (yellow pixels) was formed, as shown in Fig. 1. By calculating the center of gravity of the cluster, we obtained the coordinate information of the hit point left by the heavy ions on the Topmetal-M chip. After passing through the Topmetal-M chip, the heavy ions continued to move forward and eventually hit the DUT (red point in Fig. 1). Using the relative position information of the two chips and the hit-point coordinate information on Topmetal-M, we determined the hit position on the DUT. Because the ions were uniformly distributed, the entire DUT was irradiated, with a uniform hit probability. Thus, the sensitive parts of the DUT were more prone to SEEs. The distribution of the sensitive map was obtained by counting the SEE events in the different parts. This sensitive map provided guidance for the radiation hardening design of the DUT.

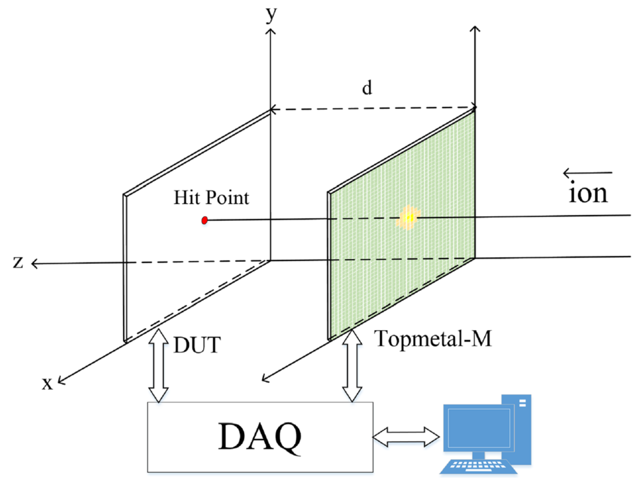

Fig. 1 Structure diagram of the prototype

Compared with heavy-ion microbeam technology, this prototype does not require special equipment to control the incident position of the beam. An unfocused heavy-ion beam can be used to locate the sensitive area because the positioning chip can provide the hit-position information of each incident particle. The purpose of microbeam focusing is to accurately control the position of the incident particle. In addition, the purpose of microbeam scanning is to control the incident particle to cover the entire chip under testing. For this prototype, we only need an unfocused heavy-ion beam to be injected into Topmetal-M and the DUT. Topmetal-M can directly provide the position information of the incident particle. Compared with the complex control of the microbeam scanning method, the prototype can achieve the locating function more succinctly. To distinguish each incident particle, the prototype has a requirement for the beam intensity, which is approximately several thousand counts/cm^2/s. Although the required beam intensity is not high, the advantage of the prototype is that it can distinguish the incident position and action area of a single particle. These results are helpful for analyzing the relationship between the number of incident particles and the occurrence of SEE in the DUT. The cluster size of Topmetal-M depends on the incident particle type and energy. It can cover dozens of pixels. Because Topmetal-M has energy resolution, we can obtain the intensity distribution map of the particle action area. Using a single particle intensity distribution map, the response of the DUT to the SEE can be analyzed more precisely.

The DAQ controls and reads data from the two chips and then transfers the data to the personal computer (PC). It provides a global clock for Topmetal-M and the DUT. Therefore, Topmetal-M and the DUT can work synchronously. The time at which the SEE of the DUT occurs (current increase for single event latchup (SEL) or logic upset for single event upset (SEU)) can be matched to the corresponding hit-position information of Topmetal-M; i.e., the prototype can retrieve a hit map captured by the positioning chip when the ions responsible for the SEE occur. Because the heavy ions must pass through the positioning chip before hitting the DUT, the material budget should be reduced to ensure that the heavy ions retain sufficient linear energy transfer (LET) when they hit the DUT. The thickness of the Topmetal-M chip fabricated by the foundry was 700 μm, and it was thinned to 70 μm to reduce the material budget for the prototype. However, it was still relatively thick in the SEE test. In future, we hope that the positioning chip can be thinned to <30 μm. Chip-thinning studies are currently underway. A thinner chip has not only the advantage of a lower material budget but also less angle scattering, which affects the position resolution. Moreover, the distance between Topmetal-M and the DUT should be minimized. This is another factor affecting the position resolution. The pixel size of the position chip was 40 μm, and one ion could fire dozens of pixels. With the use of the center-of-gravity algorithm, the position resolution can reach several microns. To obtain a higher resolution, a small pixel size can be designed in the next version of the Topmetal-M chip.

3 Hardware and firmware design of prototype

3.1 Topmetal-M

Topmetal-M is a MAPS with two operation modes: MAPS and Topmetal [21]. The chip was implemented using a 130-nm high-resistivity (> 1 kΩ cm) CMOS imaging process and thinned to 70 μm from the back side [20]. Figure 2 shows the layout and block diagram of Topmetal-M. It is a pixel chip with a large area of 18 mm × 23 mm that includes a matrix of 400 × 512 pixel cells and a periphery circuit. Each pixel cell has dimensions of 40 μm × 40 μm. The peripheral circuit was placed at the left and bottom of the pixel matrix. The chip had 169 bonding pads, which were arranged sequentially at the bottom. The pixel matrix is divided into 16 sub-arrays (400 × 32 pixels per sub-array), which can be read simultaneously. The chip was read out in the rolling shutter architecture, and the maximum clock rate was 40 MHz [20].

The circuit structure of the Topmetal-M pixel cell is shown in Fig. 3. The charge collected by the Topmetal or sensor diode was first fed into the charge-sensitive amplifier (CSA). The time constant of the CSA was adjusted by changing the bias voltage of CSA_VRST. The CSA output was divided into two paths. In the energy path, the signal directly passes through the two-stage source followers and is then buffered. In the time path, the CSA output signal is first fed into the comparator. The output of the comparator increases if the signal exceeds its threshold (COMP_VREF). The high level is maintained by peak holding and then triggers the time-to-amplitude converter (TAC) circuit. LATCHB is a control signal for switching on the TAC charging circuit, and TAC_RESET is a control signal to

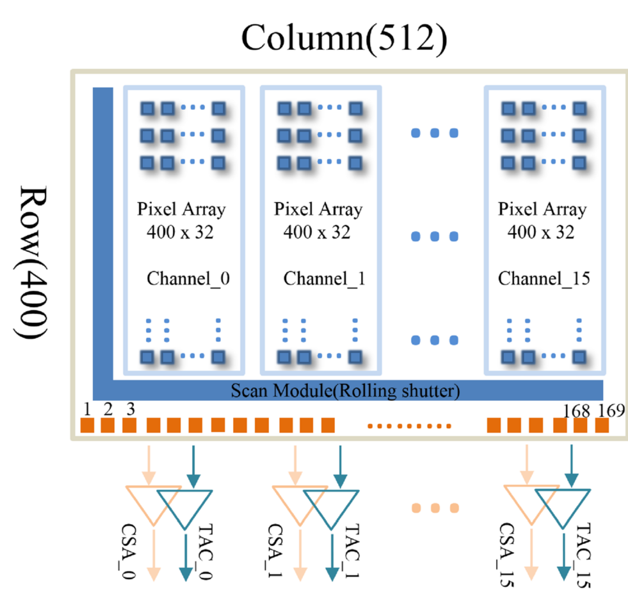

Fig. 2 Topmetal-M layout and structure diagram

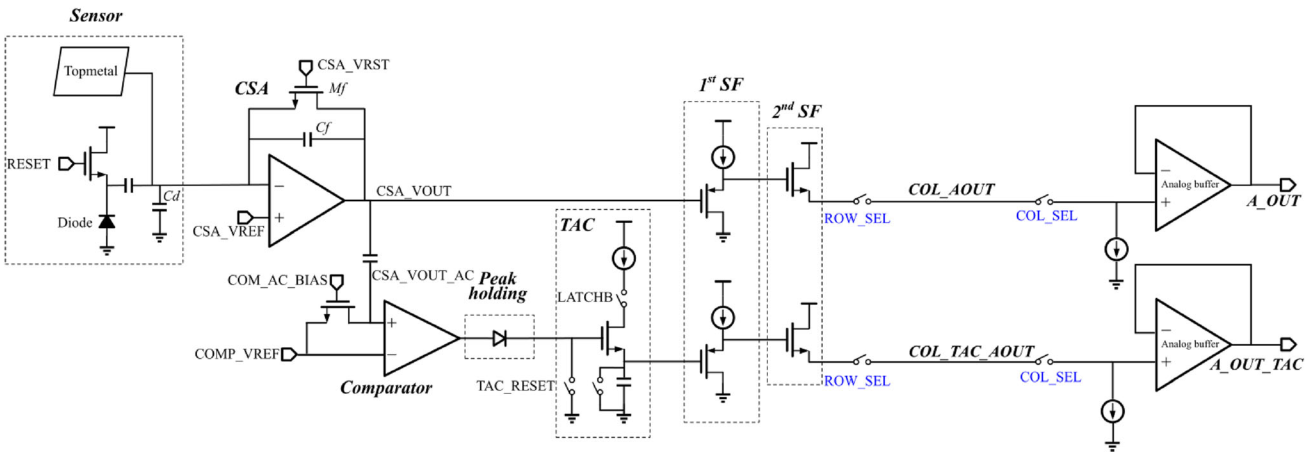

Fig. 3 Block diagram of Topmetal-M pixel cell [20, 21]

reset the TAC. The TAC output is followed by two-stage source followers and analog buffers, similar to the energy path. By reading the TAC output signal (A_OUT_TAC), we can determine the charging time and then calculate the time when a heavy ion hits the chip. The chip can provide not only energy information but also time information, which makes it useful for high-energy experiments.

3.2 Topmetal-M DAQ

The Topmetal-M DAQ is a 32-channel readout system based on peripheral component interconnect express (PCIe). Figure 4 shows the structure diagram of the readout system. It consists of a BondingBoard assembled with a single Topmetal-M chip, a MotherBoard, and a pixel readout unit (PRU) based on a Xilinx Kintex-7 field-programmable gate array (FPGA). The control commands and data transmission between the readout system and the PC are all through the PCIe interface.

3.2.1 Topmetal-M BondingBoard

The Topmetal-M BondingBoard, as shown in Fig. 5, is used for chip gluing and wire-bonding. The chip was glued at the center of the board using an epoxy resin adhesive and then wire-bonded with aluminum wires 25 μm in diameter. After the wire bonding, the other components were welded to the board. To reduce the material budget, a slot was opened on the board, directly below the sensor area of the chip. The connector between the BondingBoard and MotherBoard was a dual-row pin header.

3.2.2 Topmetal-M MotherBoard

Topmetal-M MotherBoard was between the BondingBoard and PRU and had the functions of chip power supply, bias voltage, analog output buffer, and digital signal level shift. We used a low-dropout linear regulator (LDO) for power management to reduce the noise on the board, and the power for the sensor was monitored. When the monitored current was abnormal, the LDO was automatically shut down. An 8-channel 16-bit digital-to-analog converter (DAC) can provide a bias voltage for the chip. Therefore, it is convenient to perform a bias voltage scan when testing the chip. To drive a 50 Ω coaxial cable, the analog outputs are buffered with low-noise amplifiers on the board. An oscilloscope was used to observe the waveform of the analog signals. The digital control signal of the sensor was 1.2 V, whereas the FPGA IO standard is 2.5 V; thus, level shifters were used. The digital signal

Fig. 4 Structure diagram of the Topmetal-M readout system

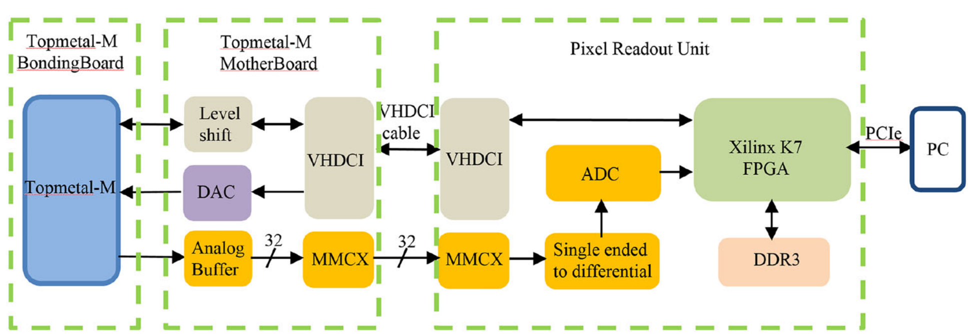

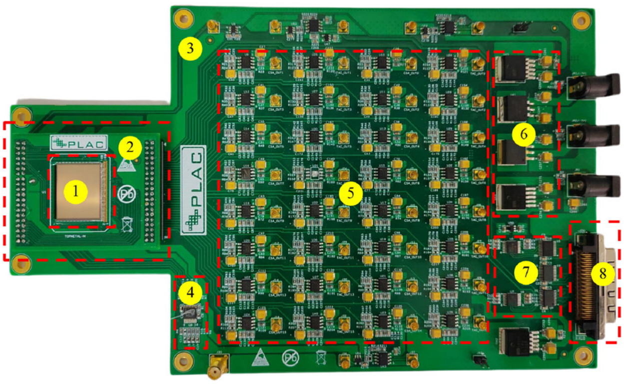

Fig. 5 Topmetal-M BondingBoard and MotherBoard.① Topmetal-M pixel sensor ② Topmetal-M BondingBoard ③ Topmetal-M MotherBoard ④8-channel DAC ⑤32-channel analog buffer ⑥LDOs ⑦Level shifters ⑧VHDCI connector

connector was a 68-pin VHDCI connector that could provide 20 pairs of differential signals.

3.2.3 PRU

The PRU was a DAQ board based on a Xilinx Kintex-7 FPGA, as shown in Fig. 6. It is designed to configure the Topmetal-M chip, convert analog signals, buffer raw data, and transfer data to the PC. The board was a 32-channel ADC card equipped with 8-lane PCIe to communicate with the PC. Single-ended analog inputs should be converted into differential signals to satisfy the input requirements of the ADC. Moreover, the DC bias of the analog inputs can be adjusted using the DAC. Two TI ADC chips (ADS52J90) were placed on the board. The ADC can be configured for 8-channel, 16-channel, and 32-channel inputs with corresponding resolutions of 10, 12, and 14 bits, respectively. For our readout system, the ADCs operated in the 16-channel, 12-bit resolution mode, and the maximum sampling rate was 80 MHz in this mode. The data interface between the ADC and FPGA was a 4-lane JESD, with a lane rate of 5 Gbps. There were four DDR3 chips with a capacity of 512 MByte on the board. The data sampled by the ADCs were transferred to the FPGA, buffered in DDR3, and then read out to the PC through 8-lane PCIe.

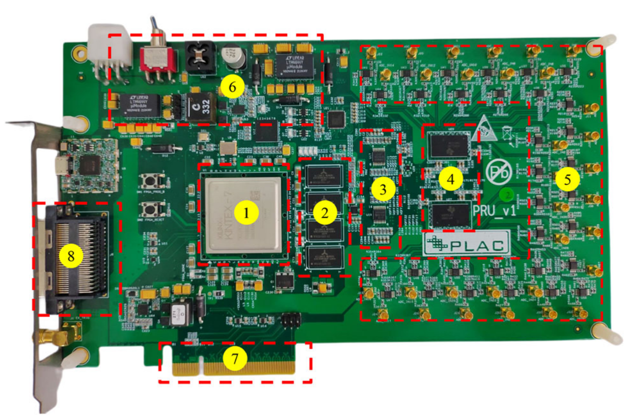

Fig. 6 PRU. ①Xilink Kintex7 FPGA ②DDR3 ③DAC ④32-channel ADC ⑤32- channel Single-ended differential circuit ⑥Power supply ⑦PCIe ⑧VHDCI stack connector

3.3 FPGA firmware design

Figure 7 shows the structure of the FPGA firmware design. It is composed of a clock management unit, control unit, and data transmission unit. An external differential crystal oscillator of 200 MHz is used as the input clock. Using the mixed-mode clock manager (MMCM) IP core, different clocks are generated for different parts. One output of the MMCM is sent to the clock generator AD9517. The AD9517 generates two clocks. One is used as the digital scan clock for Topmetal-M, and the other is used as the sampling clock for the ADC. All clocks originate from the same clock source; i.e., it is a synchronous design. The commands are sent to the FPGA through the PCIe interface. After processing by the control interface, the decoded commands are sent to the metal-M and SPI interfaces. The metal-M interface produces control signals for the Topmetal-M chip, whereas the SPI interface produces control signals for ADC, DAC, and AD9517. The data sampled by the ADCs are first sent to the ADC interface. After serial-to-parallel conversion, the data are processed by a data package unit and then saved in DDR3 using the DDR controller. When the FPGA receives the command for data transmission, the DDR controller reads the data from DDR3 and sends the data to the PCIe controller. The PCIe controller then transmits the data to the PC through the PCIe interface.

4 Beam tests and results

We evaluated the performance of the SEE localization system prototype based on a Topmetal-M pixel sensor under heavy-ion beams at HIRFL. The tests and results are discussed in this section.

The Topmetal-M chip has a matrix of 400 $\times$ 512 pixel cells. Owing to a design error in the digital module, only 128 $\times$ 512 pixels, which were distributed directly at the top of the chip, could be scanned properly. The matrix was divided into 16 channels (128 $\times$ 32 pixels per channel), and all channels could be read out simultaneously. The digital scan clock range of Topmetal-M was 1-40 MHz. After data processing and comparison, it was found that the chip could achieve an optimal effect with a scan clock of 10 MHz. Therefore, the digital scan clock was set to 10 MHz

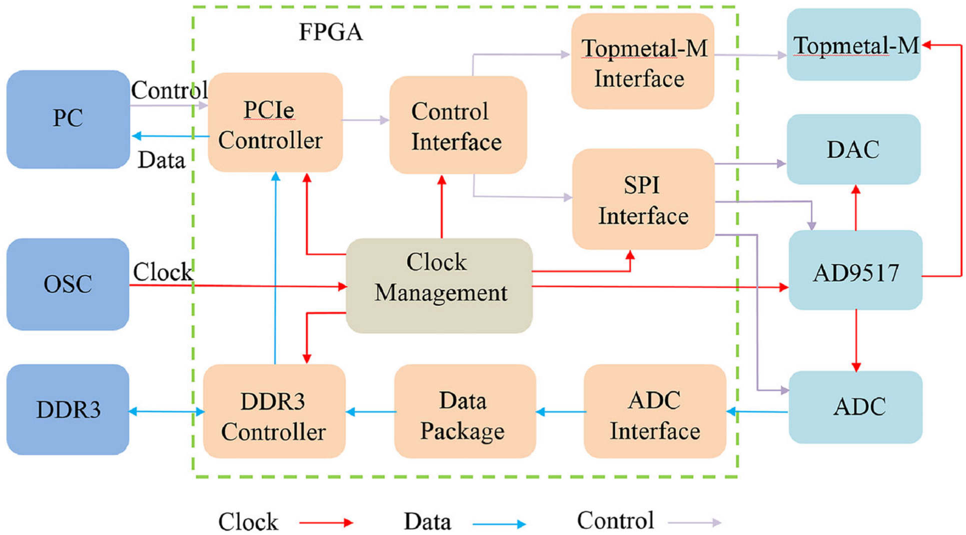

Fig. 7 FPGA firmware design

for all the test results presented in this paper. The frame rate of the chip was 2.44 kHz with this scan clock. The analog outputs of Topmetal-M were sampled by a 12-bit ADC with a sampling clock of 40 MHz, which was generated from the same source as the digital scan clock. Thus, each pixel had four sampling points. Figure 8 shows the ADC sampling waveform of the signal. The value of the third sampling point on a pixel was the most stable point during pixel switching and was used as the value of the current pixel.

4.1 Beam test setup

Beam tests were performed at room temperature at the beam terminal of HIRFL. Two sets of BondingBoard with Topmetal-M chips were plugged into the two MotherBoards separately. Two MotherBoards were overlapped through the positioning holes on the board, and they were separately connected to one PRU by the VHDCI cable. Thus, Topmetal-M chips were placed in parallel, and the horizontal distance between them was approximately 3 cm. The front Topmetal-M chip was used as the positioning chip, and the other was used as the DUT. As the test circuit boards required high stability, we fixed them on a heavy metal platform, which reduced the vibration.

Figure 9 shows the beam test platform. The Ar40 beam emitted from the terminal had an energy of 320 MeV/u, and the average beam intensity was several thousand counts/cm^2/s. The prototype was fixed to an XYZ stage. Using an infrared calibrator, the Topmetal-M chip were roughly adjusted to the beam terminal emitting center. Thus, the beam could be injected vertically into the center of the chip. After field debugging, the background noise level of the chip was aggravated by the surrounding electronic instruments. Therefore, the PRU and the PC were placed under the experimental platform far from the chip and the MotherBoard to reduce noise. To reduce vibration,

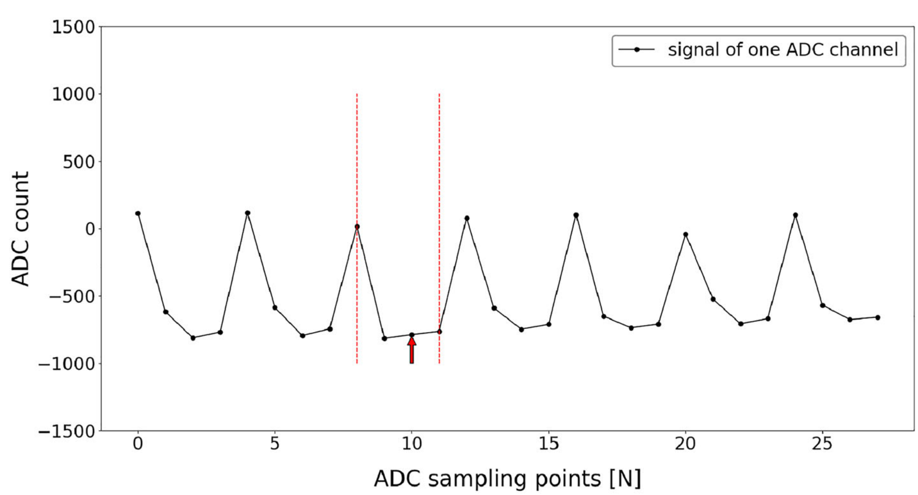

Fig. 8 ADC sampling waveform of the signal

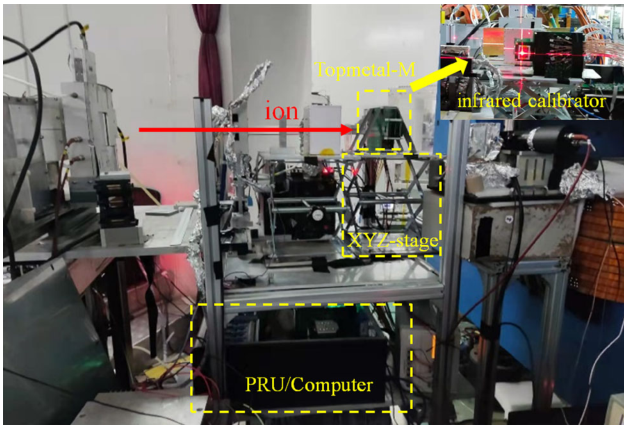

Fig. 9 Beam test platform at HIRFL

all the test circuit boards were fixed on a heavy metal platform.

4.2 Signal-cluster size and amplitude

In the beam test, we used the MAPS feature to collect the charge. When particles passed through the depletion region in the pixel sensor, they generated electron-hole pairs. The electrons shifted to the n-well owing to thermal diffusion and were collected by several neighboring pixels. The charge signal was converted into a voltage signal by the CSA circuit and then read to the off-chip. The input dynamic range of the ADC was -1 to 1 V, and the sampling resolution was 12 bits; thus, the minimum scale of the ADC was approximately 0.49 mV. As the charge conversion gain of Topmetal-M is approximately 78.6 $\mu V/e^-$ [20], we can determine the collected charge of the signal from the ADC value. The data acquired by the ADC were transmitted to the PC through the PCIe interface. Through ADC sampling, the signal for one pixel was converted into a one-dimensional discrete time series Pix_T. For the entire pixel array, we obtained a three-dimensional matrix of $Pix_M \times Pix_N \times Pix_T$. Pix_M represents the row number of the pixel array, Pix_N represents the column number of the pixel array, and Pix_T represents the frame number of the pixel array.

Figure 10 shows the typical signal cluster of one particle, which lasted for approximately six consecutive frames. The shape of the signal cluster approximated a three-dimensional Gaussian wave packet. The signal amplitude decayed on a frame-by-frame basis. If sliced from the timeline, which implies looking at each frame, the shape of the signal is close to a circle. When we focus on one pixel in the signal cluster, the waveform of the signal amplitude is as shown in Fig. 11. The signal appears suddenly, rises to the maximum amplitude, and then decays over the next few frames.

Here, we introduce the method and process for obtaining a single signal from the data matrix. The main idea of the algorithm is to regard a single signal cluster as the same connected component and then find different connected components in the data matrix. First, we set the threshold for each pixel. If the value of the pixel was below the threshold, we set the value to zero. If the value was above the threshold, we kept it unchanged. Subsequently, we performed a first-order difference operation along the time axis. Values greater than zero were reserved, and all others were set to zero. Only the first frame was preserved for each signal cluster. Then, we extracted different signals through the connected components and calculated other signal information.

By counting the pixels in the first frame of a signal cluster, we determined the size of the cluster. Figure 12 shows the distribution of the signal-cluster size. For one signal cluster, the number of fired pixels was mostly between 40 and 93, and Gaussian fitting indicated a mean value of 66 pixels. Furthermore, there were signal clusters with >100 fired pixels. This condition was mainly caused by overlapping signals.

We could determine the amplitude of one signal cluster by summing the amplitude values of all the pixels in the signal cluster. Figure 13 presents the distribution of the signal-cluster amplitudes. As shown, the distribution range is wide. The Bethe-Bloch formula describes the average energy loss of charged particles when they travel through matter. For a charged particle in a thin absorbing layer, the distribution of the energy loss due to ionization can be accurately described by the Landau distribution. As the depletion layer of the Topmetal-M chip was approximately 10 μm, the energy deposition of the particle was fitted by a Landau distribution [22]. The Landau fitting indicated that the most probable value was approximately 43632 e^-.

4.3 Angular and position resolution

As mentioned previously, the two pixel sensors were placed in parallel, and the beam was incident perpendicular to the chip. In addition to the information of a single signal cluster, we obtained the correlation information between the signals on the two pixel sensors. Figure 14 shows the signal clusters in two pixel sensors in the same frame. The pixel sensor closer to the beam (the top one in the figure) had more signal clusters. When the particles pass through the pixel sensor in front, they may lose all their energy and be unable to hit the second one. In addition, as indicated by the signals marked in the figure, the two signals produced by the same particle had different locations on the two pixel sensors. There are two main reasons for this finding. First, the particle changes its direction of motion owing to its interaction with the pixel sensor. Second, there is an

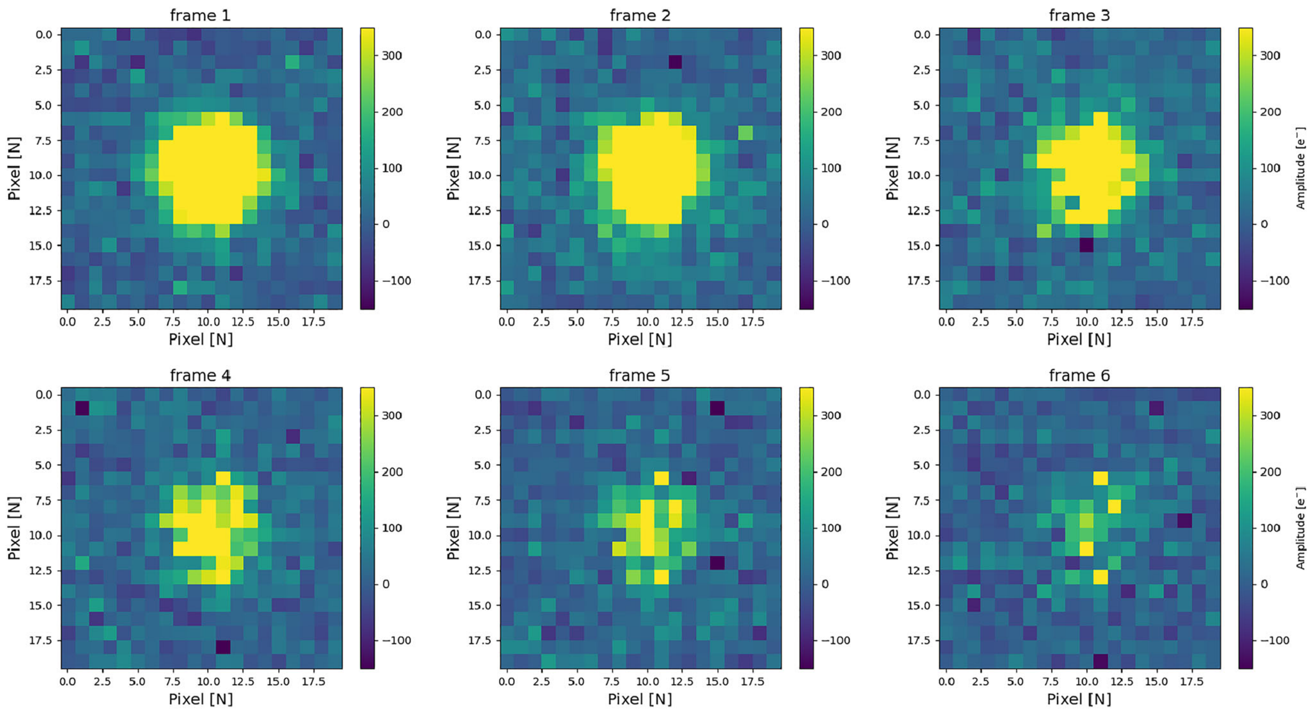

Fig. 10 Signal cluster with six consecutive frames

Fig. 11 One pixel in the signal cluster

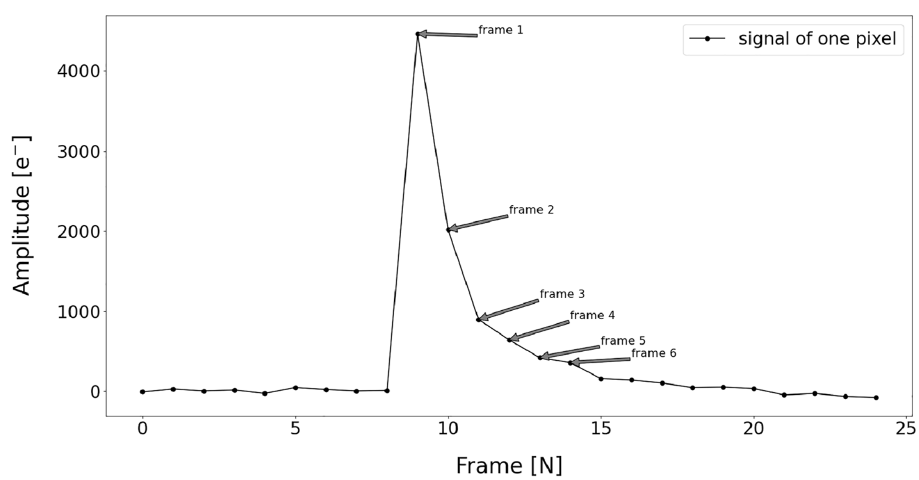

offset angle between the incident direction of the beam and the direction perpendicular to the chip surface.

The offset angle of the particle should be calculated to accurately locate the sensitive region on the DUT to SEEs. We can determine the angle deviation according to the position of the energy deposition generated by the same particle incident on the two pixel sensors. As the particle hits the two pixel sensors almost simultaneously, we can obtain the signal cluster on the two pixel sensors in the same frame (as shown in Fig. 14). We define x_i and y_i as the coordinates of the fired pixels in one signal cluster, e_i represents the charge of each pixel, and n represents the total number of fired pixels. Thus, the center of gravity of the signal cluster is given by Eq. (1).

$$X_{\mathrm{C}} = \frac{\sum_{i=1}^{n} x_i \cdot e_i}{\sum_{i=1}^{n} e_i}, \quad Y_{\mathrm{C}} = \frac{\sum_{i=1}^{n} y_i \cdot e_i}{\sum_{i=1}^{n} e_i} \tag{1}$$

The deflection angle of the two signal clusters can then be determined by calculating the coordinates of the two centers of gravity and the distance between the two pixel sensors. Figure 15 shows the distribution of the deflection angle. The inherent deflection angle of the prototype to the beam was 1.7°, and the angular resolution was 0.6°. As mentioned previously, the inherent deflection angle can be regarded as the offset angle between the incident direction

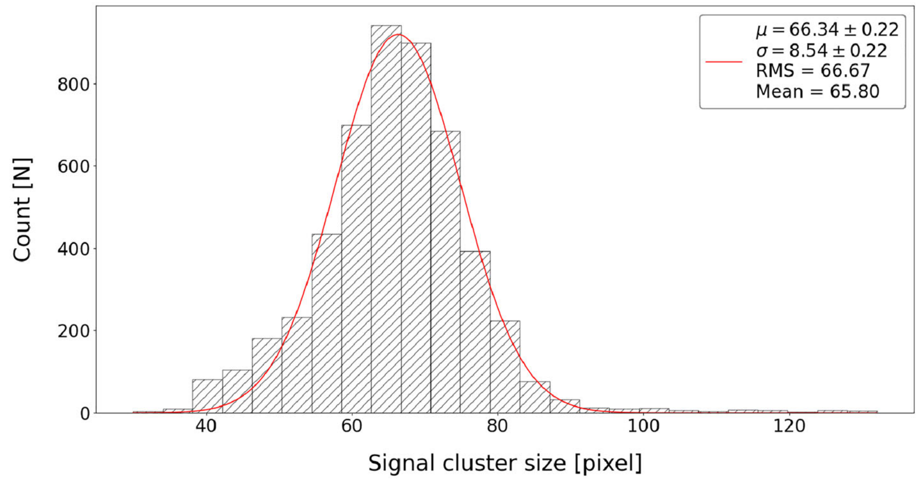

Fig. 12 Distribution of the signal-cluster size in the beam test

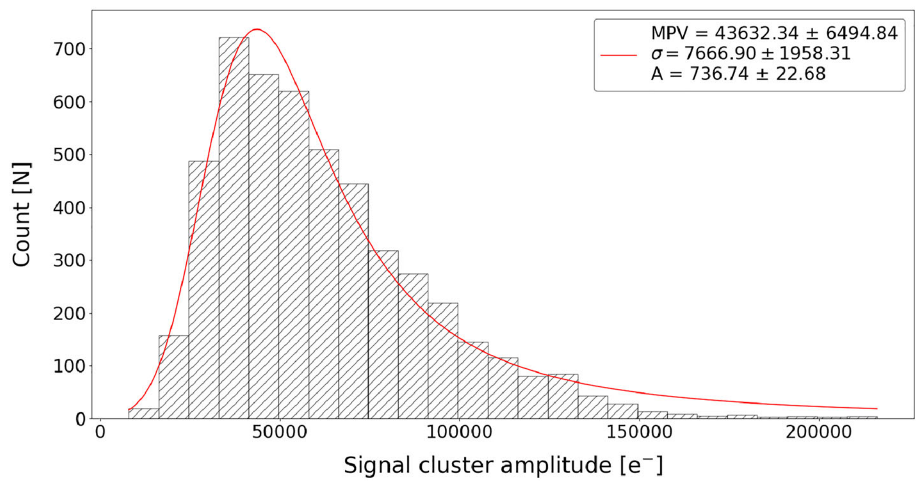

Fig. 13 Distribution of the signal-cluster amplitude in the beam test

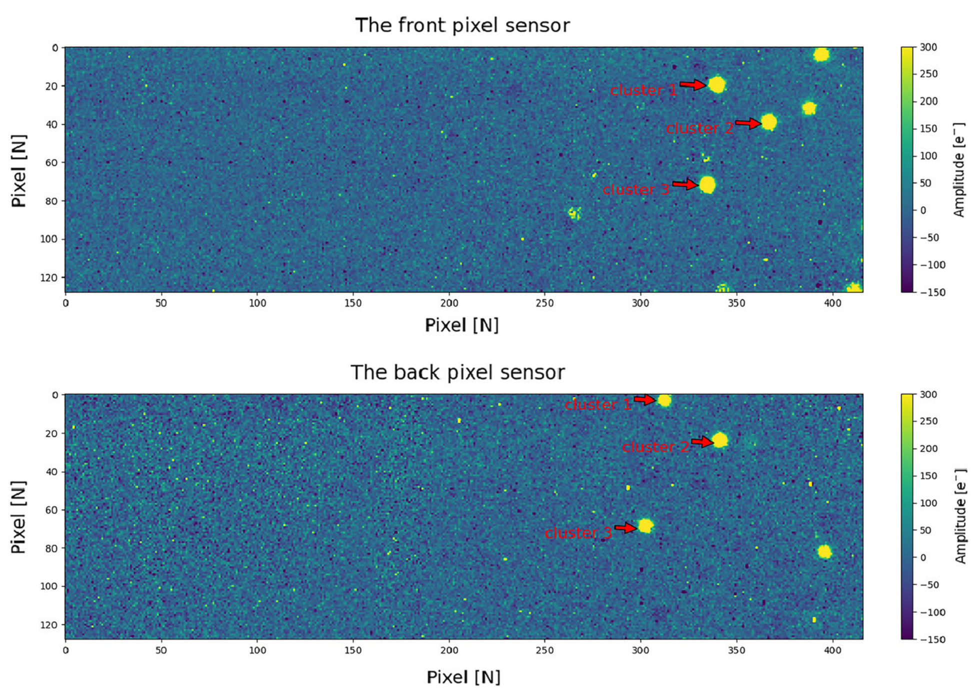

Fig. 14 Signal cluster in two pixel sensors

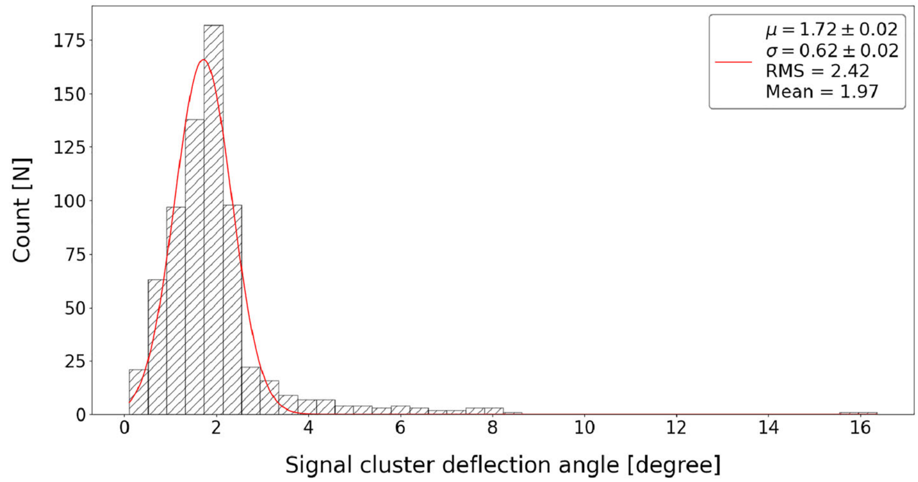

Fig. 15 Distribution of the deflection angle in the beam test

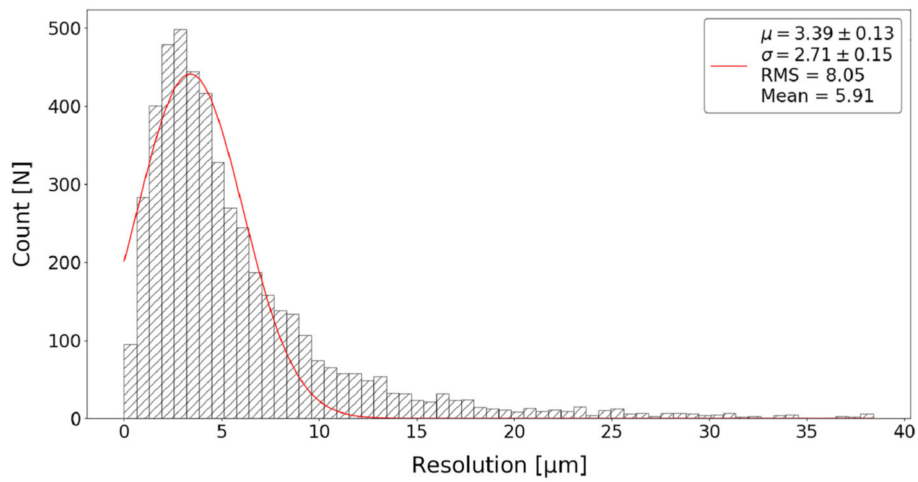

Fig. 16 Distribution of the spatial resolution in the beam test

of the beam and the direction perpendicular to the chip surface. Another angle is the statistical fluctuations caused by particle deflection. Owing to the high energy of the particles, the angular deflection is small.

To calculate the spatial resolution of this localization system, the first two frames of the same signals were selected first. Then, Eq. (1) was used to determine the centers of gravity of the clusters in the first and second frames, i.e., X_{c1}, Y_{c1} and X_{c2}, Y_{c2}, respectively. The resolution was calculated using the equation $\sqrt{(X_{c1} - X_{c2})^2 + (Y_{c1} - Y_{c2})^2}$. As shown in Fig. 16, the Gaussian fitting gave a spatial resolution of 3.4 µm.

5 Conclusion and outlook

Pulsed laser technology has the advantages of a low cost, a high temporal resolution, a high spatial resolution, and high-density charge injection. However, the interaction mechanisms between the laser and heavy ions are different. Heavy-ion microbeam technology also has a high spatial resolution; however, the test system is complex, and the test efficiency is low. In this study, a prototype for SEE localization with a CMOS pixel sensor was developed, and a 32-channel readout system based on PCIe was designed for this prototype. The prototype uses an unfocused heavy-ion beam and does not require special equipment to control the incident position of the beam. Thus, the prototype was relatively simple. The prototype can provide the position information and action area of each incident particle. Heavy-ion beam tests were performed at HIRFL. The results indicated that the prototype can successfully distinguish each incident particle and can be used for SEE localization. The mean size of one particle was 66 pixels, and the distribution of the total charge of each signal was close to the Landau distribution. The inherent deflection angle of the prototype to the beam was 1.7°, and the angular resolution was 0.6°. The prototype can also localize heavy ions at a position resolution of 3.4 µm. In the next version of the Topmetal-M chip design, the digital scan error was fixed. The chip was implemented using a high-voltage CMOS imaging process, which reduced the degree of diffusion of electrons produced by ionization. Moreover, the pixel size was smaller. The thickness of the chip was reduced to reduce the material budget and angle scattering. These improvements will increase the spatial resolution in future.

Acknowledgements We also thank HIRFL for hosting the physical measurements of the prototype.

Author Contributions All authors contributed to the study conception and design. Material preparation, data collection and analysis were performed by Jun Liu, Shi-Qiang Zhou and Zhuo Zhou. The first draft of the manuscript was written by Jun Liu and all authors commented on previous versions of the manuscript. All authors read and approved the final manuscript.

References

1. W.T. Yang, X.C. Du, Y.H. Li et al., Single-event-effect propagation investigation on nanoscale system on chip by applying heavy-ion microbeam and event tree analysis. Nucl. Sci. Tech. **32**, 106 (2021). https://doi.org/10.1007/s41365-021-00943-6
2. R.G. Alia, M. Brugger, S. Danzeca et al., Single event effects in high-energy accelerators. Semicond. Sci. Technol **32**, 034003 (2017). https://doi.org/10.1088/1361-6641/aa5695
3. Z.L. Yang, X.H. Wang, H. Su et al., Experimental study on heavy ion single-event effects in flash-based FPGAs. Nucl. Sci. Tech. **27**, 7 (2016). https://doi.org/10.1007/s41365-016-0015-8
4. J. Mekki, M. Brugger, R.G. Alia et al., CHARM: a mixed field facility at CERN for radiation tests in ground, atmospheric, space and accelerator representative environments. IEEE Trans. Nucl. Sci. **63**, 2106–2114 (2016). https://doi.org/10.1109/TNS.2016.2528289
5. Z.L. Li, Y. Fan, Z. Wang et al., A new method for directly locating single-event latchups using silicon pixel sensors in a gas detector. Nucl. Instrum. Methods B **962**, 163697 (2020). https://doi.org/10.1016/j.nima.2020.163697
6. C. Cai, T.Q. Liu, X.Y. Li et al., Heavy-ion and pulsed-laser single event effects in 130-nm CMOS-based thin/thick gate oxide anti-fuse PROMs. Nucl. Sci. Tech. **30**, 80 (2019). https://doi.org/10.1007/s41365-019-0602-6
7. C. Gu, R. Chen, G. Belev et al., Application of two-photon-absorption pulsed laser for single-event-effects sensitivity mapping technology. Materials (2019). https://doi.org/10.3390/ma12203411
8. N.A. Dodds, N.C. Hooten, R.A. Reed et al., SEL-sensitive area mapping and the effects of reflection and diffraction from metal lines on laser SEE testing. IEEE Trans. Nucl. Sci. **60**, 2550–2558 (2013). https://doi.org/10.1109/TNS.2013.2246189
9. M. Mauguet, D. Lagarde, F. Widmer et al., Single events induced by heavy ions and laser pulses in silicon Schottky diodes. IEEE Trans. Nucl. Sci. **65**, 1768–1775 (2018). https://doi.org/10.1109/TNS.2018.2813096
10. S. Buchner, N. Roche, J. Warner et al., Comparison of single event transients generated at four pulsed-laser test facilities-NRL, IMS, EADS. JPL. IEEE Trans. Nucl. Sci. **59**, 988–998 (2012). https://doi.org/10.1109/TNS.2012.2201956
11. G.H. Du, J.L. Guo, R.Q. Wu et al., The data acquisition and beam control system at the IMP microbeam facility. Nucl. Instrum. Methods B **306**, 29–34 (2013). https://doi.org/10.1016/j.nimb.2012.11.034
12. J.L. Guo, G.H. Du, J.S. Bi et al., Development of single-event-effects analysis system at the IMP microbeam facility. Nucl. Instrum. Methods B **404**, 250–253 (2017). https://doi.org/10.1016/j.nimb.2017.02.012
13. W.T. Yang, X.C. Du, J.L. Guo et al., Preliminary single event effect distribution investigation on 28 nm SoC using heavy ion microbeam. Nucl. Instrum. Methods B **450**, 323–326 (2019). https://doi.org/10.1016/j.nimb.2018.09.038
14. T. Kamiya, K. Takano, T. Satoh et al., Microbeam complex at TIARA: Technologies to meet a wide range of applications. Nucl. Instrum. Methods B **269**, 2184–2188 (2011). https://doi.org/10.1016/j.nimb.2011.02.043
15. T. Hirono, M. Barbero, P. Breugnon et al., CMOS pixel sensors on high resistive substrate for high-rate, high-radiation environments. Nucl. Instrum. Meth. A **831**, 94–98 (2016). https://doi.org/10.1016/j.nima.2016.01.088
16. A. Dorokhov, G. Bertolone, J. Baudot et al., High resistivity CMOS pixel sensors and their application to the STAR PXL detector. Nucl. Instrum. Methods A **650**, 174–177 (2011). https://doi.org/10.1016/j.nima.2010.12.112
17. S. Mattiazzo, I. Aimo, J. Baudot et al., Beam test results of a monolithic pixel sensor in the 0.18μm tower-jazz technology with high resistivity epitaxial layer. Nucl. Instrum. Methods A **796**, 19–22 (2019). https://doi.org/10.1016/j.nima.2015.04.024
18. M. Mager, ALPIDE, the Monolithic Active Pixel Sensor for the ALICE ITS upgrade. Nucl. Instrum. Methods A **824**, 434–438 (2016). https://doi.org/10.1016/j.nima.2015.09.057
19. P. Yang, W.P. Ren, X.M. Sun et al., A monolithic active pixel sensor prototype for the CEPC vertex detector. Nucl. Instrum. Method A **924**, 82–86 (2019). https://doi.org/10.1016/j.nima.2018.10.006
20. W.P. Ren, W. Zhou, B.H. You et al., Topmetal-M: A novel pixel sensor for compact tracking applications. Nucl. Instrum. Method A **981**, 164557 (2020). https://doi.org/10.1016/j.nima.2020.164557
21. H.B. Yang, H.L. Zhang, C.S. Gao et al., Hi'Beam-S, a monolithic silicon pixel sensor based prototype particle tracking system for HIAF. IEEE Trans. Nucl. Sci. **68**, 2794–2800 (2021). https://doi.org/10.1109/TNS.2021.3128542
22. L. Landau, On the energy loss of fast particles by ionization. Sov. Phys. J. **3**, 97 (1944)